Front. Mech. Eng. 2021, 16(3): 580–592
https://doi.org/10.1007/s11465-021-0633-7

RESEARCH ARTICLE

Wei HAN, Fengzhou FANG

Orientation effect of electropolishing characteristics of 316L stainless steel fabricated by laser powder bed fusion

Abstract 3D metal printing process has attracted increasing attention in recent years due to advantages, such as flexibility and rapid prototyping. This study aims to investigate the orientation effect of electropolishing characteristics on different surfaces of 316L stainless steel fabricated by laser powder bed fusion (L-PBF), considering that the rough surface of 3D printed parts is a key factor limiting its applications in the industry. The electropolishing characteristics on the different surfaces corresponding to the building orientation in selective laser melting are studied. Experimental results show that electrolyte temperature has critical importance on the electropolishing, especially for the vertical direction to the layering plane. The finish of electropolished surfaces is affected by the defects generated during L-PBF process. Thus, the electropolished vertical surface has higher surface roughness *Sa* than the horizontal surface. The X-ray photoelectron spectroscopy spectra show that the electropolished horizontal surface has higher Cr/Fe element ratio than the vertical surface. The electropolished horizontal surface presents higher corrosion resistance than the vertical surface by measuring the anodic polarization curves and fitting the equivalent circuit of experimental electrochemical impedance spectroscopy.

Keywords electropolishing, laser powder bed fusion, 316L stainless steel, corrosion resistance, microstructure

Received October 27, 2020; accepted February 13, 2021

Wei HAN, Fengzhou FANG (✉)
Centre of Micro/Nano manufacturing Technology (MNMT-Dublin), University College Dublin, Dublin 4, Ireland
E-mail: fengzhou.fang@ucd.ie

Fengzhou FANG
State Key Laboratory of Precision Measuring Technology and Instruments, Laboratory of Micro/Nano Manufacturing Technology (MNMT), Tianjin University, Tianjin 300072, China

1 Introduction

Electropolishing is an efficient polishing process for metal materials in concentrated electrolytes; it generates a damage-free surface because the material is removed through anodic dissolution [1–3]. Atomic and close-to-atomic scale accuracy is possible with the electrochemical machining and electropolishing method because the material is removed atom by atom in the anodic dissolution [4–6]. Electropolishing of the surfaces fabricated by laser powder bed fusion (L-PBF) has been reported as an effective method to improve the surface roughness [7–9] and remove the outmost layer with residual stress without causing thermal and mechanical stress [10,11]. Lyczkowska-Widlak et al. [12] compared the electropolished and ground 316L SS samples fabricated by L-PBF and reported that electropolishing increased the corrosion resistance of sample considerably compared with grinding. Zhang et al. [13] studied the electropolishing of L-PBF-fabricated Inconel 718 part surfaces and found that the electropolishing enables to dissolve the hardening phase and relieve residual stress, resulting in lower nanohardness and elastic modulus. Urlea and Brailovski [14,15] studied the electropolishing of L-PBF-fabricated Ti-6Al-4V and IN625 multiple surfaces, which were oriented with respect to the power bed under different angles from 0° to 135°. All the surfaces were electropolished to a lower surface roughness independent of the different surface roughness caused by the changed angle. L-PBF-fabricated components suffer from process-induced imperfections, such as high residual stresses and micropores [16,17]. Residual stresses and micropores are the main reasons for the failure and low performance of some alloys fabricated by L-PBF under fatigue loading. Electropolishing was used to measure residual stresses with different depths generated by the L-PBF process to remove the sample surface layer [10,11,18]. This condition is due to the material removal performed by anodic dissolution, which generates a damage-free surface in the absence of thermal and mechanical stress [3].

Mechanical properties of 316L SS fabricated by L-PBF show anisotropic characterization and have greatly attracted the interest of researchers [19–22]. Alsalla et al. [20] fabricated 316L SS with different building orientations, measured the fracture toughness, and found that the presented defects, such as pores and cracks, were influenced by the different building orientations, thereby affecting fracture toughness, strength, and total elongation. Mertens et al. [19] performed uniaxial tensile testing on samples fabricated with different main orientations with respect to the same orientation direction. The mechanical behavior showed a strong anisotropy, which was related to the microstructures and processing conditions. Ni et al. [23] clarified the mechanical properties of 316L SS fabricated by L-PBF using tensile experiments and reported the anisotropy properties closely related to the grain sizes and boundaries, which were dissimilar in the different surfaces with respect to the building orientation. Kong et al. [21] reported that a lower resistance to deformation along the building orientation of 316L SS fabricated by L-PBF was confirmed because most grain boundaries were parallel to the loading direction.

The corrosion behavior of 316L SS fabricated by L-PBF is influenced by the microstructures, which can be optimized by adjusting the process parameters, such as the scanning speed and laser power. Voids or international porosities are generally formed in the L-PBF process under two completely different conditions of insufficient [24,25] and excessive heat input [26]. The insufficient heat input leads to lack-of-fusion voids, and the excessive heat input leads to keyhole-induced pores. A lower energy density or large scanning space causes less overlap or even no overlap between scanning lines, resulting in changes in the wetting and thermal conditions of the melt pool. If the molten material fails to wet the previous layer and/or hatch line, lack-of-fusion voids form because the molten material is insulated by surrounding powder [24]. Keyhole-induced porosities are mostly formed due to occurrence of local cod zones with higher surface tension and insignificant recoil pressure, and a parametric study has shown that a keyhole is formed when exceeding a certain threshold of input power [27]. Finer microstructures and minimum manufacturing defects could be obtained during the L-PBF of 316L SS by adjusting the scanning speed, thereby leading to better biocompatibility due to the increase in corrosion resistance and decrease in toxicity ion release [28]. In general, fast scanning speeds generated more voids, inside of which oxide power and nonmelt silicon were found. Therefore, the number of pitting sites increased with increasing scanning speed due to pits that occurred preferentially at the voids [29]. 316L SS showed improved corrosion resistance and biocompatibility when fabricated by L-PBF at high laser power, and more subgrain boundary and dislocation were found in the L-PBF-fabricated sample than the wrought 316L SS, thereby promoting the formation of passive film to better corrosion resistance [30]. The influence of L-PBF parameters on the anisotropic properties of fabricated parts has been widely studied [31,32], and many studies [33,34] focused on the mechanical properties and corrosion behavior of L-PBF parts. However, reports about the influence of orientation effect on the electropolishing process of L-PBF 316L SS parts were few.

The distinction in electropolishing characteristics on different surfaces of 316L SS fabricated by selective laser melting is studied. Different surfaces corresponding to the building orientation are electropolished, and the surface finish, surface composition of the passive oxide layer, and corrosion resistance are investigated. This study can be used to understand the anisotropy in corrosion resistance on different surfaces of 316L SS fabricated by L-PBF although the sample is electropolished. Thus, the knowledge gap in the anisotropy study on the different surfaces of 316L SS fabricated by L-PBF is filled.

2 Experimental approach

316L SS samples were fabricated by L-PBF with the stainless-steel CL 20ES powders (316L) (Concept Laser, Lichtenfels, Germany). The laser power was 100 W, and the scanning speed was 600 mm/s. The layer thickness was 25 μm. The laser spot size and scanning space were 50 and 84 μm, respectively. The sample size was designed as 10 mm × 20 mm × 2 mm for electropolishing. The unpolished surface of the sample was insulated from the electrolyte by coating with an aerosol conformal coating (RS Components, Ltd., UK). The study on electropolishing original 316L SS surface fabricated by L-PBF is presented separately. This study is focused on the electropolishing characteristics of the different surfaces corresponding to the orientation direction. Therefore, the polishing side was uniformly ground with 600 grit abrasive sandpaper to smoothen the rough surface obtained from L-PBF. The electrolyte for electropolishing consisted of H_2SO_4 (98%), H_3PO_4 (85%), and glycerol in the volume ratio of 5:4:1, which has shown good electropolishing effect for 316L SS in the previous research [1,35]. All the electrolyte compositions were purchased from the Mistral Industrial Chemicals, UK. The NaCl solution in the concentration of 3 mol/L was used for all the electrochemical analysis at room temperature. Each electrochemical measurement was repeated at least three times for higher credibility. Figure 1 shows the experimental setup, and the details can be found in the previous research [1,35]. The electropolishing potential was supplied by a potentiostat/galvanostat CS310, which was also used for the electrochemical analysis. The hotplate stirrer was used to heat the electrolyte and cooperated with a thermal sensor to control the electrolyte temperature. A magnetic stir bar was used to stir the electrolyte with the speed range of 100–2000 r/min. The samples were cleaned using distilled water and ethanol

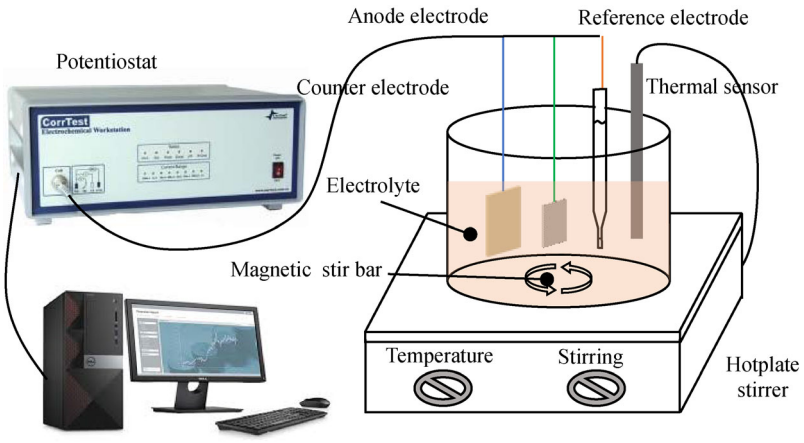

Fig. 1 Experimental setup used for the electropolishing and electrochemical analysis.

in sequence in an ultrasonic agitation bath for 3 min before the electropolishing process. The electrochemical impedance measurement was carried out on the potentiostat/galvanostat CS310, and the measured spectra were fitted with the accessory software. VHX-5000 digital microscope, 3D optical profiler (NPFLEX), and Omicron NanoTechnology MXPS system with a dual X-ray anode (Omicron DAR 400) were used for the surface characterization.

3 Results and discussion

3.1 Electropolishing different surfaces

Figure 2 shows the schematic of the L-PBF of 316L SS, in which the building orientation is the *Z*-axis. The horizontal surface is perpendicular to the building orientation, and the vertical surface is in parallel with the building orientation. Both surfaces, horizontal and vertical surface, were electropolished in an H_2SO_4-based electrolyte, and the electrochemical analysis of electropolished surface was performed in NaCl solution.

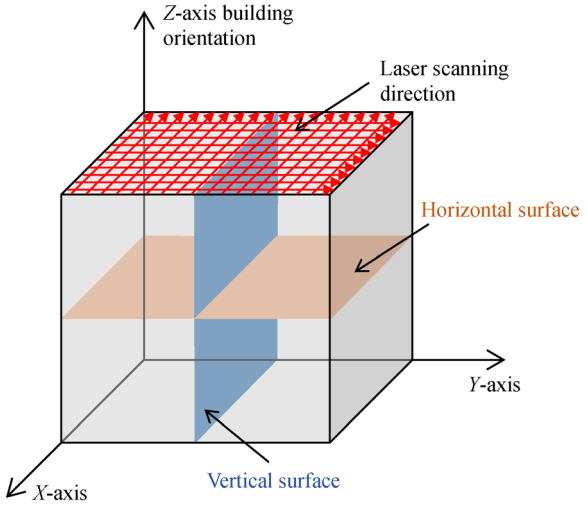

Fig. 2 Schematic of the laser powder bed fusion of 316L SS.

Figure 3 shows the polarization curves of different plans at the electrolyte temperature of 28 °C and 66 °C. Under the electrolyte temperature of 28 °C, the current density increases with increasing the applied potential in the range of 1.4 to 3 V with the vertical surface. However, a limiting current density plateau region (LCDPR) [3], where the best electropolishing effect can be obtained, can be observed evidently with the horizontal surface. In the LCDPR, the passive oxide film on the workpiece surface increases with

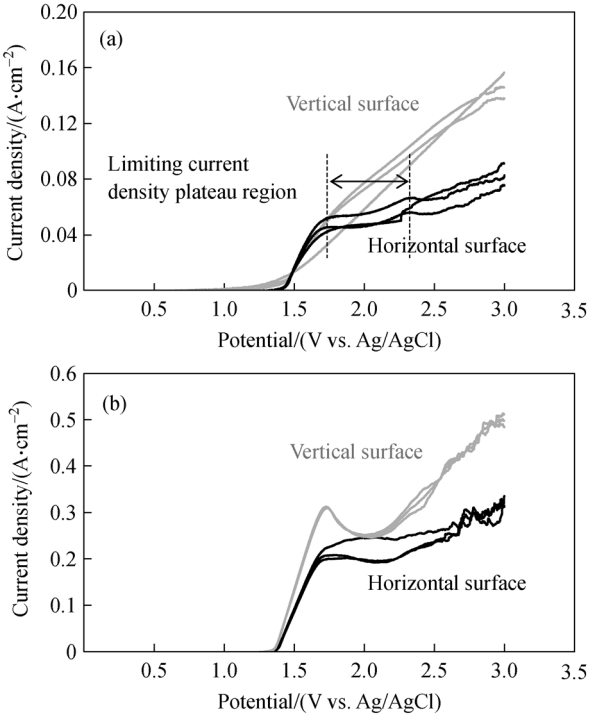

Fig. 3 Polarization curves of different plans at the electrolyte temperature of (a) 28 °C and (b) 66 °C. The stirrer speed was 667 r/min, and the scan rate of the polarization curve was 20 mV/s.

increasing applied potential, slight change in the current density. On the contrary, the thickness of passive oxide film on the vertical surface does not change with increasing applied potential under the electrolyte temperature of 28 °C, thereby increasing the current density with the potential. Under the electrolyte temperature of 66 °C, the LCDPR can be observed on the horizontal and vertical surface, as shown in Fig. 3(b). Hence, the thickness of passive oxide film on the vertical surface increases along with the applied potential in the LCDPR when the electrolyte temperature is increased to 66 °C. The potential width of the LCDPR with the vertical surface is much narrower than the horizontal surface, indicating that the stability of the passive oxide film on the horizontal surface is higher than the vertical surface. Figure 4 shows the current density transients with different plans at the electrolyte temperature of 28 °C and 66 °C with the electropolishing duration of 20 min. The applied potential of 2 V was determined by the LCDPR shown in Fig. 3 to obtain the best electropolishing effect. The current density with the vertical surface is slightly higher than the horizontal surface, which coincides with the polarization curves in Fig. 3. The current density decreases at the initial stage of electropolishing, which agrees with a traditional electropolishing process because a passivation process occurs on the sample surface [3]. A high electrolyte temperature is necessary for electropolishing vertical surface to obtain better electropolishing effect because the polarization curves of the vertical surface only show the critical LCDPR at the electrolyte temperature of 66 °C.

Figure 5 shows the electropolished horizontal and vertical surfaces with the electrolyte temperature of 66 °C. Smooth surfaces can be obtained due to the sufficient electropolishing effect, and the surface roughness *Sa* was decreased to 35 and 55.7 nm with the horizontal and vertical surface, respectively. Moreover, many defects generated by the electropolishing are shown in Fig. 5. The defects in electropolishing are normally generated by corrosion, and corrosion pits have different

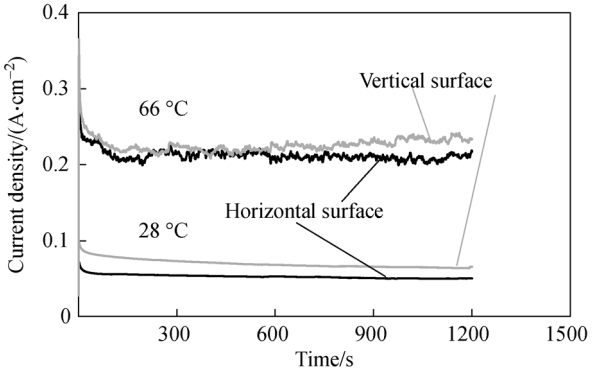

Fig. 4 Current density transients with different plans at the electrolyte temperature of 28 °C and 66 °C. The stirrer speed was 667 r/min, and the applied potential was 2 V.

appearances with the defects in Fig. 5. Hence, the defects are generated in the L-PBF process. L-PBF is a significantly complicated process because the performance is influenced by many parameters, such as laser power, layer thickness, and chamber environment. Therefore, defects are easily generated when these parameters could not be optimized effectively. Zhang et al. [36] classified the common defects in three types: Porosities, incomplete fusion, and cracks. The common defects have also been categorized in equipment-related, power-related, and processing-related defect formations [37]. Liverani et al. [38] summarized that mainly three types of defects are observed in the 316L SS fabricated by L-PBF, namely, 1) binding defects, 2) pores, and 3) layered voids. On the basis of the previous reports and the defects that appeared in this study, the observed defects are classified into two types, namely, process-related defects and gas-related defects. The defects related to the lack of fusion of powder particles are process-related defects. The particle fusion can be influenced by many processes, such as the quality and cleanness of the mirrors, laser power, and scanning speed. Unmelted particles are caused by insufficient fusion, which could result in low junction quality between adjacent layers and adjacent melt pools. The process-related defects are characterized by irregular shape and unmelted particles inside. The unmelted particle can be observed clearly in the ellipse marked as “A” in Fig. 5(b). The defects are considered gas-related defects when the formation process is related to the included gas during the solidification process. The gas between the powder particles may dissolve in the molten pool, especially when the packing density of metal powders is low. In addition, the gas solubility in the molten pools can be high because of the high molten pool temperature generated by the intense laser power. The gas-related defects are typically smaller with a spherical shape. The two types of defects can be observed on electropolished surfaces in Fig. 5. Moreover, the number of defects on the electropolished vertical surface is greater than the horizontal surface, as shown in Fig. 5. The gas-related defects are normally generated in one laser scanning layer, and the process-related defects can be generated not only in a single layer but also the interface of adjacent layers. Defect size, shape, and densification can be varied by changing the melting pool size and overlapping between neighboring melt pools during the L-PBF process [39]. For example, a shallow melt pool can be formed by changing the laser transforms from the Gaussian beam to the flat-top beam due to the uniform distribution of the energy and decreased power density [40]. This condition causes weak layer-to-layer bonds, resulting in more unfused defects.

Figures 5(a) and 5(b) show that the defect edges were smoothened by the electropolishing because the electropolishing current density concentrates on the defect edges, resulting in a higher material removal rate. To compare the original and electropolished defect edges, 316L SS

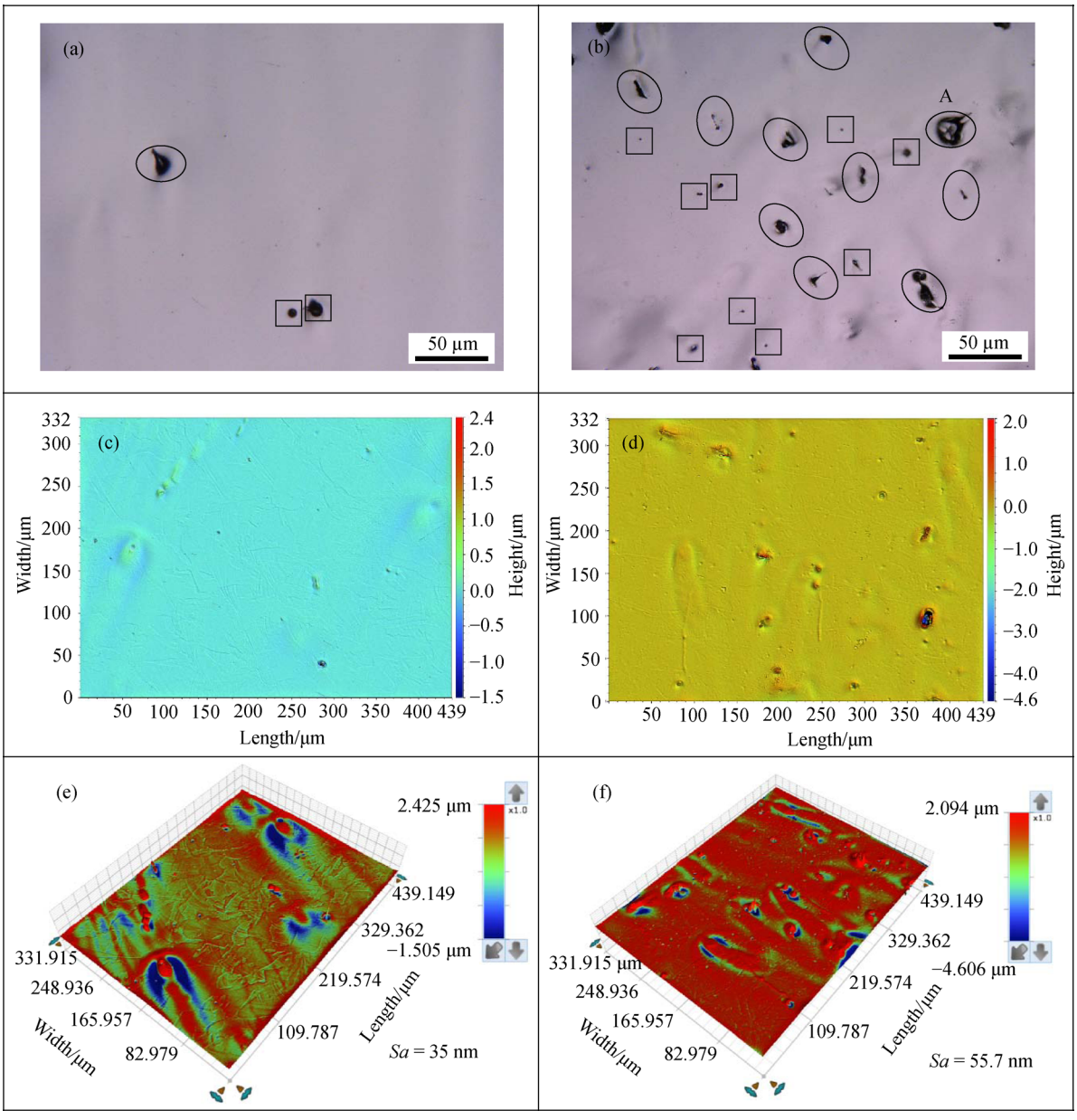

Fig. 5 Electropolished horizontal and vertical surface with the electrolyte temperature of 66 °C. The applied potential was 2 V, and the stirrer speed was 667 r/min. The electropolishing duration was 1200 s. Optical microscope image of the electropolished (a) horizontal and (b) vertical surfaces; contour image of the electropolished (c) horizontal and (d) vertical surfaces; and topography of the electropolished (e) horizontal and (f) vertical surfaces. The ellipse and square indicate the process-related defects and gas-related defects, respectively.

fabricated by L-PBF was uniformly ground with 600, 1200, and 2500 grit abrasive sandpaper in sequence, and then mechanical polished using the colloidal silica polishing suspension with micro sizes of 3 and < 1 μm. Figure 6 shows the different surfaces after grinding and mechanical polishing. The edges of defects are significantly shaped compared with the defects shown in Figs. 5(a) and 5(b), especially on the vertical surface, because electropolishing rounds the defect edges due to the higher electrochemical dissolution rate. In addition, Fig. 6 also shows that the number of defects on the vertical surface is higher than the horizontal surface, and the process-related defects are the dominant defects on the vertical surface, which are the same as the electropolished surfaces shown in Fig. 5. Therefore, electropolishing enables modifying the defect edges but not eliminating the defects. Figure 7 shows the electropolished surface roughness *Sa* from the horizontal and vertical surface with different electrolyte temperatures. The vertical surface shows a higher surface roughness *Sa* than the horizontal place because the electropolished vertical surface has a greater number of defects, as shown in Fig. 5.

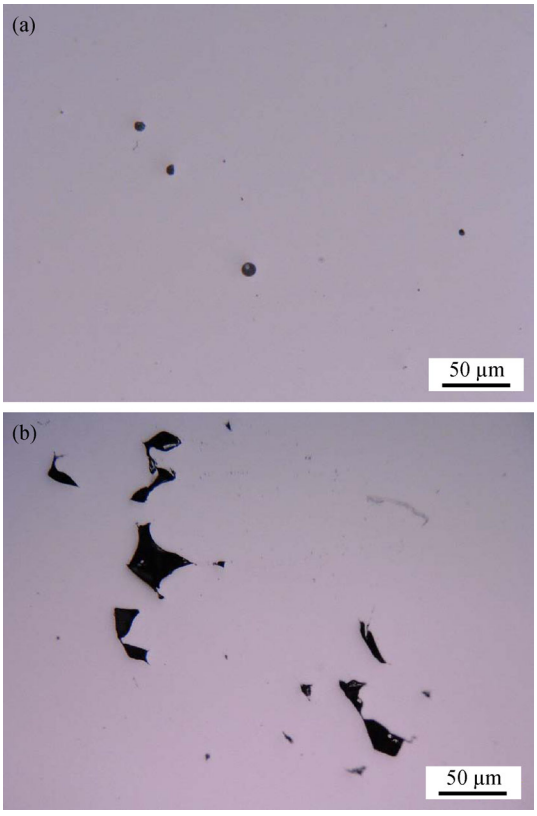

Fig. 6 Defects observed on the (a) horizontal and (b) vertical surfaces after grinding and mechanical polishing.

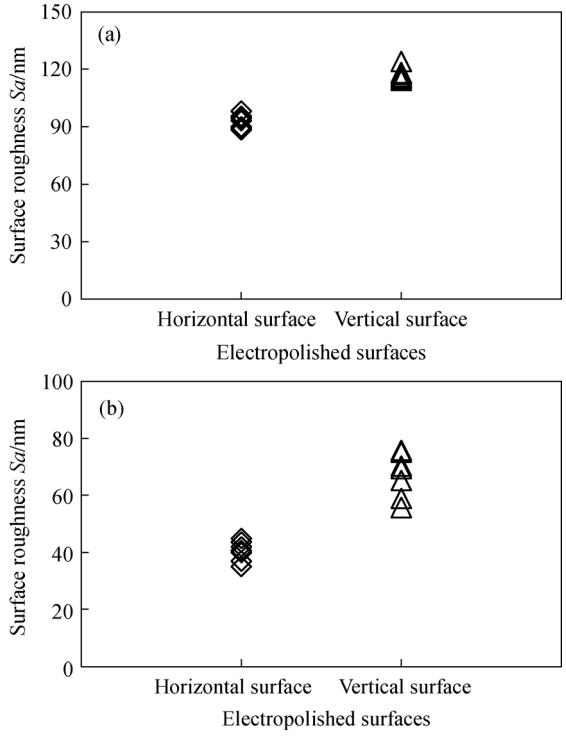

Fig. 7 Electropolished surface roughness *Sa* from the horizontal and vertical surfaces with the electrolyte temperatures of (a) 28 °C and (b) 66 °C.

3.2 X-ray photoelectron spectroscopy (XPS) spectra analysis

The compositions of different electropolished surfaces were investigated by XPS spectra. Figure 8 shows the XPS survey spectra of the electropolished different surfaces with the electrolyte temperature of 66 °C. Table 1 shows the corresponding chemical composition of the different electropolished surfaces. The O 1s element was the dominant composition for electropolished surfaces because a thick passive oxide film is formed after removing the air-formed oxide film on the workpiece surface during electropolishing [3]. The atomic percentage of the O 1s element was 29.12% on the outmost surface of the electropolished vertical surface; it was lower than the electropolished horizontal surface of 34.43%. Therefore, the electropolished horizontal surface has a thicker passive oxide film due to the higher percentage of O 1s element than the vertical surface. Moreover, the element ratio of Cr/Fe seriously affects the corrosion resistance of the electropolished surface, and higher corrosion resistance corresponds to the higher ratio of Cr/Fe [41,42]. The element ratios of Cr/Fe were 0.84 and 0.72 with the electropolished horizontal and vertical surface, respectively. Therefore, the higher corrosion resistance of the electropolished horizontal surface is expected. This finding coincides with the percentages of O 1s element on the outmost surfaces of different surfaces shown in Table 1.

Figure 9 shows the high-resolution XPS spectra of Cr and Fe elements. The Cr element exists in the forms of Cr(0), Cr_2O_3, $Cr(OH)_3$, and CrO_3 on the outmost surface of the electropolished horizontal surface. Cr(O) was obtained

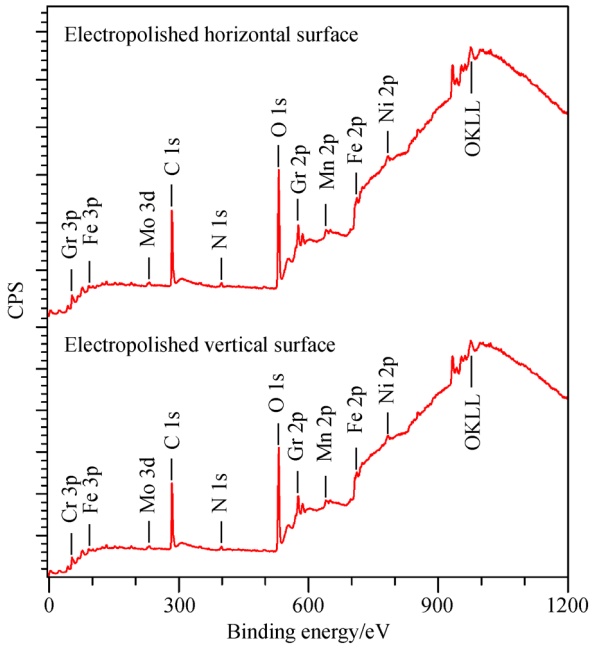

Fig. 8 XPS survey spectra of the electropolished different surfaces with the electrolyte temperature of 66 °C.

Table 1 Chemical compositions of the different electropolished 316L SS surfaces with the electrolyte temperature of 66 °C

Component name	Position	Electropolished horizontal surface		Electropolished vertical surface	
		Area	Atom/%	Area	Atom/%
O 1s	531.0	21236.09	34.43	20111.01	29.12
C 1s	284.0	9975.37	47.38	10812.08	45.87
Mn 2p	640.0	6217.98	2.12	2416.12	0.74
Si 2p	91.0	163.97	0.95	2221.74	11.54
Cr 2p	576.0	11634.10	4.74	9421.14	3.43
Ni 2p	853.0	1735.94	0.37	2051.38	0.39
Mo 3d	231.0	796.24	0.40	1056.07	0.47
P 2p	133.0	436.72	1.74	471.20	1.68
S 2p	168.0	195.94	0.55	29.73	0.08
N 1s	399.0	642.21	1.69	729.21	1.72
Fe 2p	711.0	19430.15	5.62	19231.32	4.79

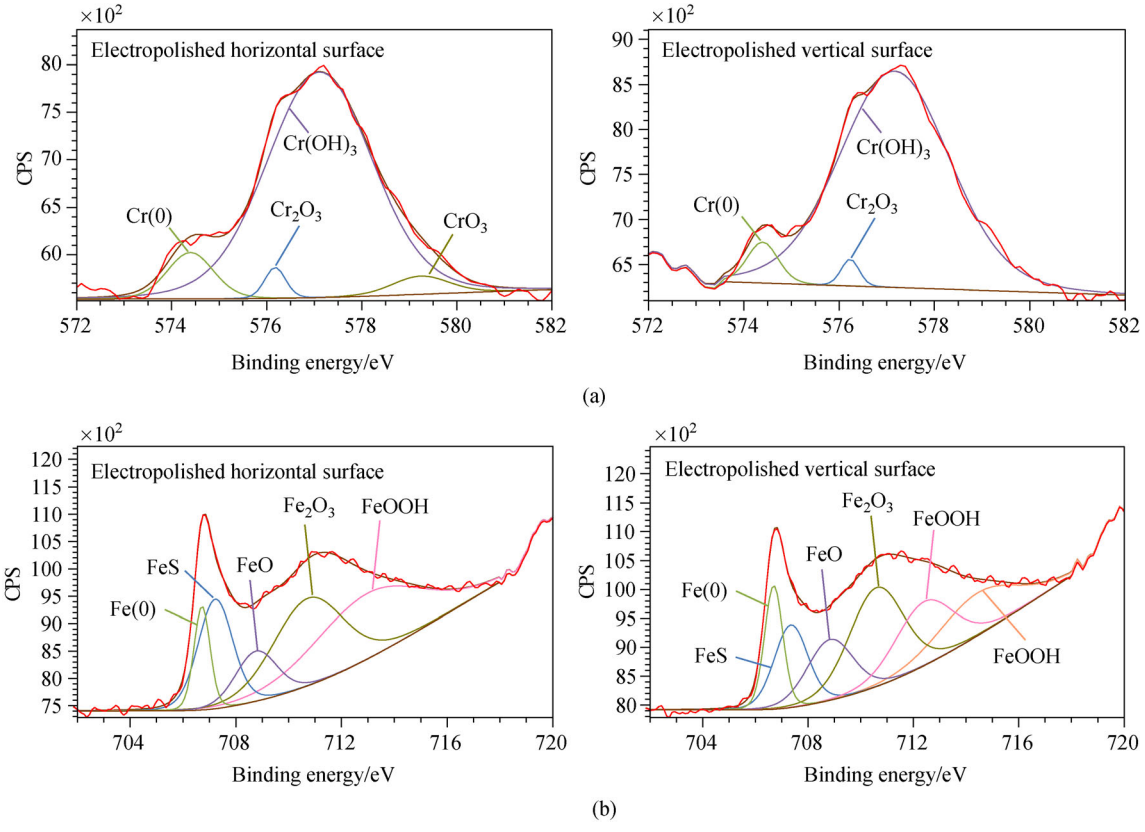

Fig. 9 High-resolution XPS spectra of chromium and iron on different electropolished surfaces. (a) High-resolution spectra of Cr; (b) high-resolution spectra of Fe.

from the original workpiece composition, and other compositions were generated from electropolishing because a passive oxide film was generated on the workpiece instead of the original film formed in the air. The dominant distribution of Cr element is in the form of $Cr(OH)_3$, which has the binding energy of 577.3 eV, for the different electropolished surfaces. This phenomenon has been reported in the previous study on electropolishing 316L SS [35]. Furthermore, CrO_3 was only measured on the electropolished horizontal surface. The CrO_3 was reported to exist in the passive oxide film of 316L SS, which is related to a high electrolyte pH and a potential drop across the oxide film [43]. The horizontal and vertical surfaces were electropolished under the same conditions.

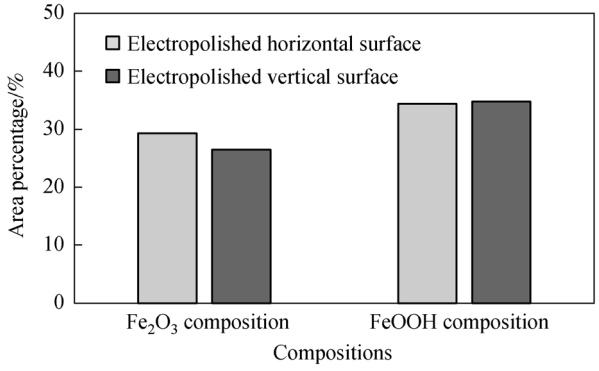

Fig. 10 Area percentages of Fe_2O_3 and FeOOH composition in the high-resolution XPS spectra of iron.

Thus, the generation of CrO_3 in the passive oxide film is also associated with the anisotropy characteristics of the workpiece. Cr^{6+} is harmful to the environment due to its toxicity property [41]. Therefore, the electropolishing of vertical surface should focus on the eco-friendly environment. High XPS resolution spectra of Iron exists in the forms of Fe(0), FeS, FeO, Fe_2O_3, and FeOOH on the different electropolished surfaces, indicating that the similar anodic dissolution reactions occur during the electropolishing of different surfaces. The peaks at a binding energy of 710.9 and 711.8 eV in Fig. 9(b) are considered the composition of Fe_2O_3 and FeOOH, respectively. The dominant Fe_2O_3 and FeOOH have similar area percentage in the high XPS spectrum of iron from the electropolished horizontal and vertical surfaces, as shown in Fig. 10. This finding verified the occurrence of similar anodic dissolution reactions in the electropolishing of different surfaces. The area percentage of Fe_2O_3 composition was much higher than that obtained from the electropolishing of commercial 316L SS [35]. This condition is due to the different manufacturing processes of the workpiece that result in the difference in the composition of the oxide film formed on electropolished surfaces.

Figure 11 shows the high-resolution spectra of oxygen on different electropolished surfaces. The measured spectra and the simulated spectra coincide with each other effectively. The O element exists in the forms of O^{2-}, M-O, Me-OH, H_2O, and OH^-. Me-OH is the dominant form of the O element, which agrees with the high-resolution XPS spectra of Cr and Fe element shown in Fig. 9. The electropolishing process has the advantage of forming a new thick passive oxide film on the polished surface, and Fig. 11 shows that the oxidized metal elements mainly existed in the form of Me-OH instead of Me-O, which was observed on the electropolished vertical surface. The M-O composition on the electropolished vertical surface might be from the formation of chromium oxide and/or iron oxides.

3.3 Corrosion resistance

Figure 12 shows the open circuit potentials (OCPs) of the electropolished horizontal and vertical surfaces measured in the 3 mol/L NaCl solution. The OCPs decreased at the initial stage because the thick passive oxide film, which was formed on the workpiece by electropolishing, was dissolved, thereby decreasing the OCP. The OCP reached a stable condition after 50 min. The OCP decreased slowly from 10 to 50 min because the rates of generation and dissolution of passive oxide film on the anode surface are close, and even the dissolution rate was slightly higher. The final stable stage could be obtained when the two rates obtain a balance, in which the generation and dissolution rates are equal. Then, the OCP shows no change even when some electrochemical reactions occur in the passive oxide film. The stable OCP is slightly higher with the electropolished horizontal plan than the vertical surface. Therefore, the electropolished horizontal surface shows slightly higher corrosion resistance than the vertical surface.

Figure 13 shows the anodic polarization scans of the electropolished horizontal and vertical surfaces measured in the NaCl solution. The corrosion potentials were -0.322 and -0.239 V with the electropolished horizontal and vertical surfaces, respectively. Therefore, the

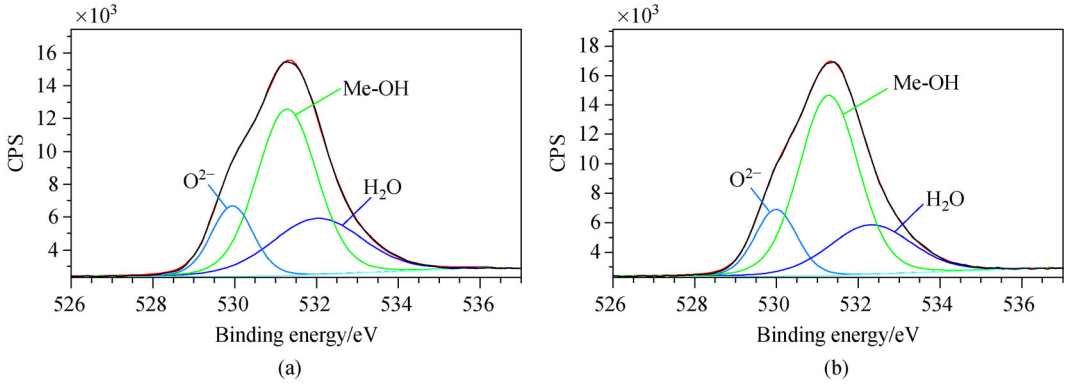

Fig. 11 High-resolution spectra of oxygen on electropolished (a) horizontal and (b) vertical surfaces.

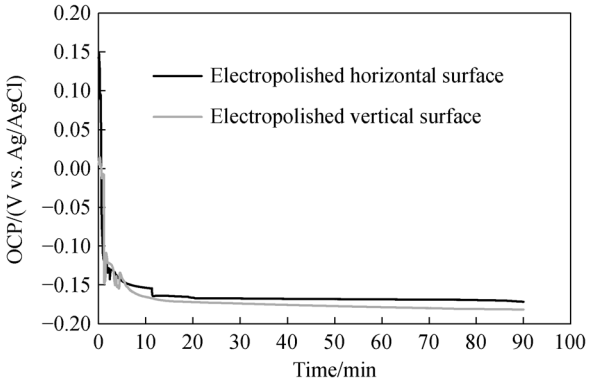

Fig. 12 Open circuit potentials (OCPs) of the electropolished horizontal and vertical surface measured in the 3 mol/L NaCl solution.

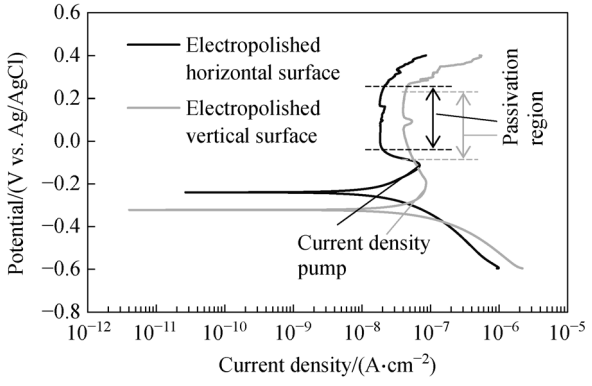

Fig. 13 Anodic polarization scans of the electropolished horizontal and vertical surfaces measured in the 3 mol/L NaCl solution. The potential range for the anodic polarization scanning was –600 to 400 mV, and the scan rate was 1 mV/s.

electropolished vertical has higher corrosion resistance in the 3 mol/L NaCl solution. A current hump is shown with each curve, thereby implying oxidation of workpiece in the NaCl solution. The current density decreased with increasing applied potential in the current hump because the thickness of passive oxide film increased. A passivation region can be seen after the current hump, and the current density is stable with increasing potential due to an increase in the thickness of passive oxide film. The current density is lower in the passivation region with the electropolished horizontal region than the vertical surface. This finding indicates that the passive oxide layer is thicker on the electropolished horizontal surface. Furthermore, Figs. 5 and 6 show that more pores are found on the vertical surface, and the defects also reduce the corrosion resistance of the electropolished vertical surface. The electropolished surfaces shown in Fig. 5 indicate that the edges of defect have a higher dissolution rate during electropolishing because the current density concentrates on the defect edges. Therefore, the corrosion resistance is reduced by the defect edges due to similar reasons. Moreover, the irregular-shaped lack-of-fusion voids have a detrimental effect on corrosion initiation and propagation compared with the keyhole-induced properties, and this effect is likely due to their crevice-like geometry [44,45]. Few lack-of-fusion voids are observed on the electropolished horizontal surface, as shown in Fig. 5, thereby also causing higher corrosion resistance of the horizontal surface.

Figure 14 shows the electrochemical impedance spectroscopy (EIS) plots of the electropolished horizontal and vertical surface measured in the NaCl solution. The workpiece was immersed in the NaCl solution for 90 min to obtain stable OPCs based on the OCPs shown in Fig. 12. Then, the EIS plots were measured and repeated three times with each workpiece. The EIS Nyquist plots show two capacitive semicircles, and the diameter is smaller with the electropolished horizontal surface in the high-frequency region. The EIS Bode plots show two time constants due to the two peaks. The first time constant is closely related to the passive oxide film on the workpiece surface, and the second one is formed due to the electric double layers between the workpiece and electrolyte. Therefore, the electrical equivalent circuit, as shown in Fig. 15, is used to simulate the measured EIS spectra with two time constants. A constant phase element (*CPE*) is used instead of a capacitor to simulate the EIS spectrum, considering that the capacitors in the EIS measurements are difficult to fit the spectra accurately. The *CPE* is expressed in Eq. (1), as follows:

$$Z_{CPE} = \frac{1}{Q(\mathrm{i}w)^n}, \tag{1}$$

where Q is a constant, n is a constant phase between 0 and 1, i is the imaginary unit, and ω is the angular frequency ($\omega = 2\pi f$, f is the frequency) [46]. *CPE* is widely used to obtain a better agreement between the theoretical and the experimentally measured EIS spectra. R_s is the electrolyte resistance, R_{ct} is the charge transfer resistance, and R_{ct} is associated with the high-frequency part of the EIS spectrum. CPE_1 and CPE_2 represent the capacitances corresponding to high and low frequency, respectively. CPE_1 is related to high-speed activities, such as the movement of charge in electric double layers. CPE_2 is mainly affected by slow processes, such as the movement of charged species through the oxide film, and R_f is the corresponding resistance [47]. The parameter values in the electrical equivalent circuit were fitted based on the measured EIS spectra, and Table 2 shows the results. The corrosion resistance can be expressed as the total resistance R_{total}, which equals to $R_{ct} + R_f$, and higher corrosion resistance is expected with larger R_{total} [48]. They were 130.157 and 104.172 kΩ·cm^2 with the electropolished horizontal and vertical surface, respectively. Therefore, the electropolished horizontal

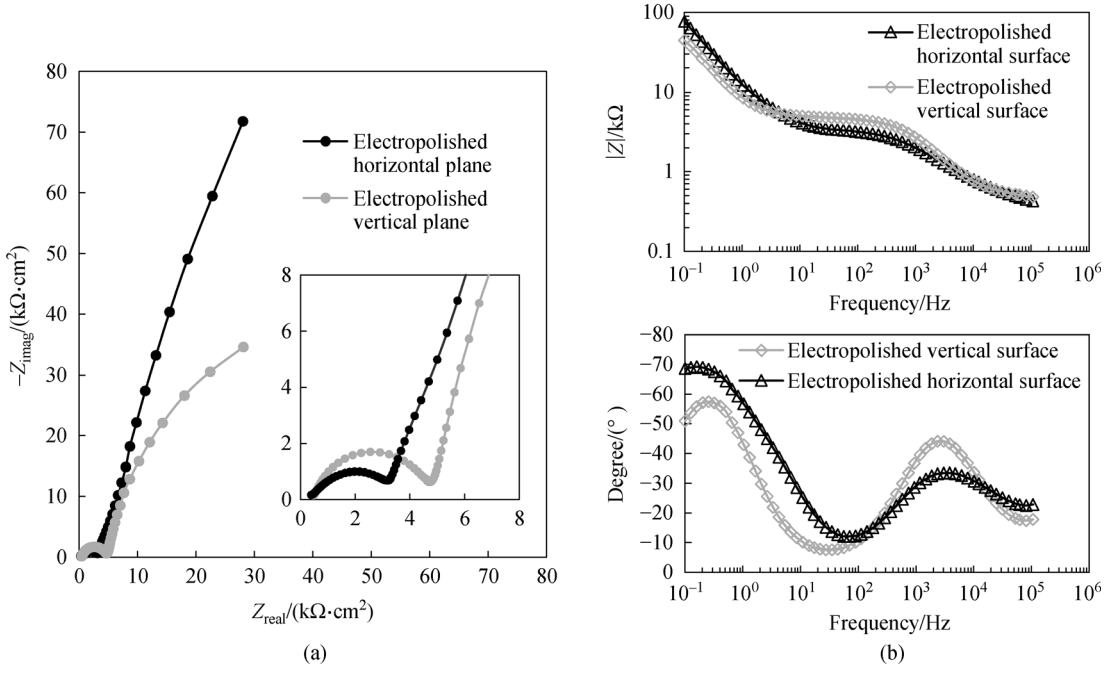

Fig. 14 EIS plots of the electropolished horizontal and vertical surface measured in the NaCl solution. The frequency range was from 100 kHz to 0.1 Hz. The AC amplitude of the applied sinusoidal signal was ±10 mV rms. (a) EIS Nyquist plots; (b) EIS Bode plots.

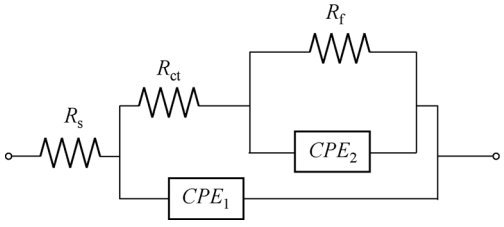

Fig. 15 Electrical equivalent circuit diagram used for EIS spectra fitting.

surface has higher corrosion resistance than the electropolished vertical surface.

3.4 Discussion

The different electropolished surfaces in Fig. 5 show that the surface finish is influenced by the L-PBF process significantly. More defects are generated on the vertical surface in L-PBF; thus, the finish of the electropolished vertical surface has higher surface roughness *Sa* than the horizontal surface, as shown in Fig. 7. Therefore, the distinction in electropolishing characteristics on different surfaces of 316L SS fabricated by L-PBF should be considered when electropolishing is selected as the post surface treatment. The XPS analysis shows that the Cr/Fe ratio, which has critical importance for the corrosion resistance of electropolished 316L SS [49], is higher on the electropolished horizontal surface than the vertical surface. The compositions of the passive oxide film on different electropolished surfaces do not have significant difference according to the high-resolution spectra of chromium, iron, and oxygen element, as shown in Figs. 9 and 11. The electrochemical analysis in the NaCl solution investigated the corrosion resistance of different electropolished surfaces through measuring the OCPs, anodic polarization, and EIS plots. According to the measured OCPs and corrosion potentials and the fitted electrical equivalent circuit for the experimental EIS, the electropolished horizontal surface has higher corrosion resistance than the vertical surface. The defects on the electropolished vertical surface, as shown in Fig. 5, may decrease the corrosion resistance in the NaCl. The defects have shown a faster anodic dissolution rate on the defect edges by comparing the electropolished and mechanical polished surfaces in Figs. 5 and 6. Moreover, the higher Cr/Fe ratio on the electropolished vertical surface, which has been

Table 2 Fitting results of the electrical equivalent circuit

Samples	R_s/Ω	CPE_1 $/(\Omega^{-1}\cdot s^n\cdot cm^{-2})$	n_1	$R_{ct}/(k\Omega\cdot cm^2)$	CPE_2 $/(\Omega^{-1}\cdot s^n\cdot cm^{-2})$	n_2	$R_f/(k\Omega\cdot cm^2)$	$R_{total}/(k\Omega\cdot cm^2)$
Electropolished horizontal surface	3.184	3.050×10^{-4}	0.793	4.057	1.921×10^{-3}	0.850	126.100	130.157
Electropolished vertical surface	4.829	2.069×10^{-4}	0.599	4.582	3.080×10^{-3}	0.896	99.590	104.172

verified by the XPS spectra in Section 3.2, also contributes to the higher corrosion resistance of the electropolished horizontal surface.

4 Conclusions

The distinction in electropolishing characteristics on different surfaces of the 316L SS fabricated by selective laser melting is studied by focusing on the polarization curve measurement during the electropolishing process and electrochemical analysis of the electropolished surfaces. The following conclusions can be drawn.

The electropolishing of different surfaces is affected by the electrolyte temperature significantly, especially for the vertical surface. A high electrolyte temperature is necessary for the optimized electropolishing effect to be obtained in the limiting current density plateau region.

The surface finish of different electropolished surfaces is affected by the defects generated in the L-PBF process, and the electropolished vertical surface has higher surface roughness *Sa* than the horizontal surface. This finding is caused by a greater number of processed-related defects generated on the vertical surface during L-PBF process.

The electropolished horizontal surface has a higher percentage of oxygen element and Cr/Fe element ratio, indicating that the electropolished horizontal surface has higher corrosion resistance than the vertical surface.

The anodic polarization curves of the electropolished horizontal and vertical surfaces show that the corrosion potential of the horizontal surface is higher than the vertical surface. Therefore, higher corrosion resistance is expected on the electropolished horizontal surface.

The EIS analysis verifies that the electropolished horizontal surface has higher corrosion resistance than the vertical surface by fitting the electrical equivalent circuit diagram of the experimental EIS.

The higher corrosion resistance of electropolished horizontal surface could be determined by a smaller number of defects and higher Cr/Fe ratio than the electropolished vertical surface.

Acknowledgements This publication has emanated from research supported in part by a grant from Science Foundation Ireland under Grant No. 15/RP/B3208. For the purpose of Open Access, the author has applied a CC BY public copyright license to any Author Accepted Manuscript version arising from this submission. This project has also received funding from the Enterprise Ireland and the European Union's Horizon 2020 Research and Innovation Program under the Marie Skłodowska-Curie Grant agreement No. 713654.

References

1. Han W, Fang F Z. Two-step electropolishing of 316L stainless steel in a sulfuric acid-free electrolyte. Journal of Materials Processing Technology, 2020, 279: 116558
2. Yang X, Yang X, Sun R, et al. Obtaining atomically smooth 4H–SiC (0001) surface by controlling balance between anodizing and polishing in electrochemical mechanical polishing. Nanomanufacturing and Metrology, 2019, 2(3): 140–147
3. Han W, Fang F Z. Fundamental aspects and recent developments in electropolishing. International Journal of Machine Tools and Manufacture, 2019, 139: 1–23
4. Fang F Z. On atomic and close-to-atomic scale manufacturing-development trend of manufacturing technology. Chinese Mechanical Engineering, 2020, 31(9): 1009–1021 (in Chinese)
5. Wang X, Han L, Geng Y, et al. The simulation and research of etching function based on scanning electrochemical microscopy. Nanomanufacturing and Metrology, 2019, 2(3): 160–167
6. Mathew P T, Rodriguez B J, Fang F Z. Atomic and close-to-atomic scale manufacturing: A review on atomic layer removal methods using atomic force microscopy. Nanomanufacturing and Metrology, 2020, 3(3): 167–186
7. Benedetti M, Torresani E, Leoni M, et al. The effect of post-sintering treatments on the fatigue and biological behavior of Ti-6Al-4V ELI parts made by selective laser melting. Journal of the Mechanical Behavior of Biomedical Materials, 2017, 71: 295–306
8. Alrbaey K, Wimpenny D I, Al-Barzinjy A A, et al. Electropolishing of re-melted SLM stainless steel 316L parts using deep eutectic solvents: 3 × 3 full factorial design. Journal of Materials Engineering and Performance, 2016, 25(7): 2836–2846
9. Mingear J, Zhang B, Hartl D, et al. Effect of process parameters and electropolishing on the surface roughness of interior channels in additively manufactured nickel-titanium shape memory alloy actuators. Additive Manufacturing, 2019, 27: 565–575
10. Simson T, Emmel A, Dwars A, et al. Residual stress measurements on AISI 316L samples manufactured by selective laser melting. Additive Manufacturing, 2017, 17: 183–189
11. Riemer A, Leuders S, Thöne M, et al. On the fatigue crack growth behavior in 316L stainless steel manufactured by selective laser melting. Engineering Fracture Mechanics, 2014, 120: 15–25
12. Lyczkowska-Widlak E, Lochynski P, Nawrat G, et al. Comparison of electropolished 316L steel samples manufactured by SLM and traditional technology. Rapid Prototyping Journal, 2019, 25(3): 566–580
13. Zhang B, Lee X, Bai J, et al. Study of selective laser melting (SLM) Inconel 718 part surface improvement by electrochemical polishing. Materials & Design, 2017, 116: 531–537
14. Urlea V, Brailovski V. Electropolishing and electropolishing-related

allowances for powder bed selectively laser-melted Ti-6Al-4V alloy components. Journal of Materials Processing Technology, 2017, 242: 1–11
15. Urlea V, Brailovski V. Electropolishing and electropolishing-related allowances for IN625 alloy components fabricated by laser powder-bed fusion. International Journal of Advanced Manufacturing Technology, 2017, 92(9–12): 4487–4499
16. Mercelis P, Kruth J P. Residual stresses in selective laser sintering and selective laser melting. Rapid Prototyping Journal, 2006, 12(5): 254–265
17. Monroy K, Delgado J, Ciurana J. Study of the pore formation on CoCrMo alloys by selective laser melting manufacturing process. Procedia Engineering, 2013, 63: 361–369
18. Leuders S, Thöne M, Riemer A, et al. On the mechanical behaviour of titanium alloy TiAl6V4 manufactured by selective laser melting: Fatigue resistance and crack growth performance. International Journal of Fatigue, 2013, 48: 300–307
19. Mertens A, Reginster S, Contrepois Q, et al. Microstructures and mechanical properties of stainless steel AISI 316L processed by selective laser melting. Materials Science Forum, 2014, 783–786: 898–903
20. Alsalla H H, Smith C, Hao L. Effect of build orientation on the surface quality, microstructure and mechanical properties of selective laser melting 316L stainless steel. Rapid Prototyping Journal, 2018, 24(1): 9–17
21. Kong D, Ni X, Dong C, et al. Anisotropy in the microstructure and mechanical property for the bulk and porous 316L stainless steel fabricated via selective laser melting. Materials Letters, 2019, 235: 1–5
22. Ahmadi A, Mirzaeifar R, Moghaddam N S, et al. Effect of manufacturing parameters on mechanical properties of 316L stainless steel parts fabricated by selective laser melting: A computational framework. Materials & Design, 2016, 112: 328–338
23. Ni X Q, Kong D C, Wen Y, et al. Anisotropy in mechanical properties and corrosion resistance of 316L stainless steel fabricated by selective laser melting. International Journal of Minerals Metallurgy and Materials, 2019, 26(3): 319–328
24. Gong H, Rafi K, Gu H, et al. Analysis of defect generation in Ti–6Al–4V parts made using powder bed fusion additive manufacturing processes. Additive Manufacturing, 2014, 1–4: 87–98
25. Bruna-Rosso C, Demir A G, Previtali B. Selective laser melting finite element modeling: Validation with high-speed imaging and lack of fusion defects prediction. Materials & Design, 2018, 156: 143–153
26. King W E, Barth H D, Castillo V M, et al. Observation of keyhole-mode laser melting in laser powder-bed fusion additive manufacturing. Journal of Materials Processing Technology, 2014, 214(12): 2915–2925
27. Bayat M, Thanki A, Mohanty S, et al. Keyhole-induced porosities in laser-based powder bed fusion (L-PBF) of Ti6Al4V: High-fidelity modelling and experimental validation. Additive Manufacturing, 2019, 30: 100835
28. Shang Y, Yuan Y, Li D, et al. Effects of scanning speed on *in vitro* biocompatibility of 316L stainless steel parts elaborated by selective laser melting. International Journal of Advanced Manufacturing Technology, 2017, 92(9–12): 4379–4385
29. Ni X Q, Kong D C, Wu W, et al. Corrosion behavior of 316L stainless steel fabricated by selective laser melting under different scanning speeds. Journal of Materials Engineering and Performance, 2018, 27(7): 3667–3677
30. Kong D, Ni X, Dong C, et al. Bio-functional and anti-corrosive 3D printing 316L stainless steel fabricated by selective laser melting. Materials & Design, 2018, 152: 88–101
31. Wen S, Li S, Wei Q, et al. Effect of molten pool boundaries on the mechanical properties of selective laser melting parts. Journal of Materials Processing Technology, 2014, 214(11): 2660–2667
32. Shayesteh Moghaddam N, Saghaian S E, Amerinatanzi A, et al. Anisotropic tensile and actuation properties of NiTi fabricated with selective laser melting. Materials Science and Engineering A, 2018, 724: 220–230
33. Kong D, Dong C, Ni X, et al. Mechanical properties and corrosion behavior of selective laser melted 316L stainless steel after different heat treatment processes. Journal of Materials Science and Technology, 2019, 35(7): 1499–1507
34. Ni X, Kong D, Wu W, et al. Corrosion behavior of 316L stainless steel fabricated by selective laser melting under different scanning speeds. Journal of Materials Engineering and Performance, 2018, 27(7): 3667–3677
35. Han W, Fang F Z. Electropolishing of 316L stainless steel using sulfuric acid-free electrolyte. Journal of Manufacturing Science and Engineering, 2019, 141(10): 101015
36. Zhang B, Li Y, Bai Q. Defect formation mechanisms in selective laser melting: A review. Chinese Journal of Mechanical Engineering, 2017, 30(3): 515–527
37. Sola A, Nouri A. Microstructural porosity in additive manufacturing: The formation and detection of pores in metal parts fabricated by powder bed fusion. Journal of Advanced Manufacturing and Processing, 2019, 1(3): e10021
38. Liverani E, Toschi S, Ceschini L, et al. Effect of selective laser melting (SLM) process parameters on microstructure and mechanical properties of 316L austenitic stainless steel. Journal of Materials Processing Technology, 2017, 249: 255–263
39. Kuo C N, Chua C K, Peng P C, et al. Microstructure evolution and mechanical property response via 3D printing parameter development of Al–Sc alloy. Virtual and Physical Prototyping, 2020, 15(1): 120–129
40. Nie X, Chen Z, Qi Y, et al. Effect of defocusing distance on laser powder bed fusion of high strength Al–Cu–Mg–Mn alloy. Virtual and Physical Prototyping, 2020, 15(3): 325–339
41. Kimbrough D E, Cohen Y, Winer A M, et al. A critical assessment of chromium in the environment. Critical Reviews in Environmental Science and Technology, 1999, 29(1): 1–46
42. Lee S J, Lai J J. The effects of electropolishing (EP) process parameters on corrosion resistance of 316L stainless steel. Journal of Materials Processing Technology, 2003, 140(1–3): 206–210
43. Luo H, Su H, Dong C, et al. Passivation and electrochemical behavior of 316L stainless steel in chlorinated simulated concrete pore solution. Applied Surface Science, 2017, 400: 38–48
44. Laleh M, Hughes A E, Yang S, et al. Two and three-dimensional characterisation of localised corrosion affected by lack-of-fusion pores in 316L stainless steel produced by selective laser melting. Corrosion Science, 2020, 165: 108394

45. Schaller R F, Mishra A, Rodelas J M, et al. The role of microstructure and surface finish on the corrosion of selective laser melted 304L. Journal of the Electrochemical Society, 2018, 165(5): C234–C242
46. Jorcin J B, Orazem M E, Pébère N, et al. CPE analysis by local electrochemical impedance spectroscopy. Electrochimica Acta, 2006, 51(8–9): 1473–1479
47. Shahryari A, Omanovic S, Szpunar J A. Electrochemical formation of highly pitting resistant passive films on a biomedical grade 316LVM stainless steel surface. Materials Science and Engineering C, 2008, 28(1): 94–106
48. Habibzadeh S, Li L, Shum-Tim D, et al. Electrochemical polishing as a 316L stainless steel surface treatment method: Towards the improvement of biocompatibility. Corrosion Science, 2014, 87: 89–100
49. Han W, Fang F Z. Eco-friendly NaCl-based electrolyte for electropolishing 316L stainless steel. Journal of Manufacturing Processes, 2020, 58: 1257–1269